Polarization Mode Dispersion of Installed Fibers

Misha Brodsky, *Member, IEEE*, Nicholas J. Frigo, *Fellow, IEEE*, Misha Boroditsky, *Senior Member, IEEE*, and Moshe Tur, *Fellow, IEEE*

Invited Paper

***Abstract*—Polarization mode dispersion (PMD), a potentially limiting impairment in high-speed long-distance fiber-optic communication systems, refers to the distortion of propagating optical pulses due to random birefringences in an optical system. Because these perturbations (which can be introduced through manufacturing imperfections, cabling stresses, installation procedures, and environmental sensitivities of fiber and other in-line components) are unknowable and continually changing, PMD is unique among optical impairments. This makes PMD both a fascinating research subject and potentially one of the most challenging technical obstacles for future optoelectronic transmission. Mitigation and compensation techniques, proper emulation, and accurate prediction of PMD-induced outage probabilities critically depend on the understanding and modeling of the statistics of PMD in installed links. Using extensive data on buried fibers used in long-haul high-speed links, the authors discuss the proposition that most of the temporal PMD changes that are observed in installed routes arise primarily from a relatively small number of "hot spots" along the route that are exposed to the ambient environment, whereas the buried shielded sections remain largely stable for month-long time periods. It follows that the temporal variations of the differential group delay for any given channel constitute a distinct statistical distribution with its own channel-specific mean value. The impact of these observations on outage statistics is analyzed, and the implications for future optoelectronic fiber-based transmission are discussed.**

***Index Terms*—Communication systems, optical fiber communication, optical fiber dispersion, optical fiber polarization.**

I. Introduction

FIBER optics revolutionized telecommunications over two decades ago, spurred by the promise of a low-loss transmission medium with seemingly infinite bandwidth. However, as the bandwidths of transported signals rapidly increased in the late 1980s, birefringence, which is a dependence of refractive index on the state of polarization (SOP), became recognized as a new impairment. Essentially, if the transit times for an optical fiber pulse were different for the x and y polarizations, for example, then an optical pulse launched in an arbitrary SOP would create two time-displaced replicas at the receiver, introducing distortion errors. As pulse widths became shorter with higher bandwidths, this differential time displacement, called differential group delay (DGD, defined later), became more injurious. Even more troubling was the recognition that this impairment varied from fiber-to-fiber (even in the same lot), from wavelength to wavelength for a given fiber at any given time, and even at each wavelength over time. For carriers, this randomness begs the question of how to assess the likelihood that any given fiber will suffer an outage for a given system. Since billions of dollars of fiber were installed before these problems surfaced, and transmission rates are likely to increase, it is clear that this problem has enduring economic implications.

Early views of these issues were fleshed out in the late 1980s and early 1990s, the impairment became known as "polarization mode dispersion" (PMD), and research has continued to the present (the term PMD is also used to quantify the phenomenon by the introduction of a *PMD vector,* to be defined in Section II). As a measure of the maturity of the field, there have been several reviews [1], [2] (including one of over 130 pages [3]) since the earliest work of Poole and Wagner [4] as well as two recent books [5], [6] concerned with PMD: the theoretical foundations are well established.

During the telecom bubble, the temporary overbuild of fiber routes with low-PMD fibers allowed the widespread deployment of 10 Gb/s systems, mitigating the need for immediate PMD compensation. For a while, most carriers seemed to have enough recent vintage fiber to satisfy the increasing demand of their customers using multiple wavelength-division-multiplexed channels to form terabit per second links. However, as the telecommunications industry comes out from a long downturn, there is a renewed interest in PMD as "good" fibers have been cherry picked on existing routes and even better fiber is needed for the worldwide deployment of 40 Gb/s systems that has already begun.

PMD-related research can be roughly divided in seven overlapping subfields, each involving both theoretical and experimental work.

1) *Development of low-PMD fiber.* The PMD coefficient of the fiber, having units of picosecond per square root kilometer, is roughly proportional to the fiber birefringence and inversely proportional to the birefringence correlation length. The former parameter has been improved by better control over the drawing process, and the latter was shortened dramatically by the introduction of so-called

Manuscript received September 18, 2006.

M. Brodsky is with AT&T Labs Research, Middletown, NJ 07748 USA.

N. J. Frigo is with the Physics Department, U.S. Naval Academy, Annapolis, MD 21402 USA.

M. Boroditsky is with the Statistical Arbitrage Group, Knight Equity Markets, Jersey City, NJ 07310 USA.

M. Tur is with the Faculty of Engineering, Tel Aviv University, Tel Aviv 69978, Israel.

Color versions of Figs. 1–4 and 6–16 are available online at http://ieeexplore.ieee.org.

Digital Object Identifier 10.1109/JLT.2006.885781

spun fibers. By twisting the fiber in the drawing process, one dramatically increases the rate at which the birefringence axis changes its orientation along the fiber. That leads to a faster randomization and to significantly lower PMD coefficients, down to 0.01 ps/km$^{1/2}$.

2) *Faithful emulation of PMD.* For system testing purposes, it is highly impractical to wait for a rare instance of high PMD in a fiber. Therefore, PMD emulators, for which any value of PMD may be programmed at will, are used for testing single-channel systems. For multichannel testing, it is important that the PMD correlation among the channels be close enough to that in the real fiber. It remains an open question of whether emulators are adequate to study the interaction of nonlinear and polarization effects.
3) *Modulation formats and receiver impact.* From the earliest days, it was clear that the return-to-zero (RZ) modulation format would be more robust to uncompensated PMD links than nonreturn-to-zero (NRZ) formats. Later, the robustness of other formats such as carrier-suppressed RZ and duobinary formats was studied. The interaction of PMD with nonlinearities adds another dimension to the problem.
4) *In-service monitoring of PMD and PMD-induced penalties.* The evolution of the magnitude and direction of the PMD vector is driven by temperature variation indoors, as well as outdoors, changes in the stress level in cables, and technical crew activities. When the bit error rate in a system increases, it is therefore desirable to be able to tell whether the system performance degradation is caused by PMD or other deleterious effects. Several methods have been developed for in-service estimation of the PMD-induced penalty. Various measurable quantities can be used for that purpose, including eye opening, synchronous and asynchronous histograms, degree of polarization, various frequency components, and frequency-resolved SOP traces.
5) *PMD compensation by optical and electronic means.* PMD compensation techniques can be categorized by the location of the device (input, output, distributed), its tracking speed, and the number of degrees of freedom. Optical techniques have been developed that introduce a compensating PMD (with only a few degrees of freedom) to cancel a large measure of a link's PMD at a given wavelength, but the problem for multiple wavelengths is still an issue. Electronic methods center on tapped delay lines and delayed decision techniques at the receiver to infer the transmitted signal. While it must be implemented at each receiver, this approach uses integrated electronics, whose speed and processing power keep increasing. PMD compensation has gone a long way to reach a status where it is quite well developed in terms of understanding the requirements, laboratory demonstrations, and some field tests. However, at present, there seems to be no commercially viable multichannel solution.
6) *System aspects of PMD:* calculation and measurement of outage statistics, development of optimal PMD avoidance strategies, etc. Historically, there have been three distinct system approaches to PMD mitigation. If the PMD is low, it can be ignored. For a medium severity of PMD, the problem can be avoided either by cherry picking good fiber among the available fiber strands in a cable or letting higher logical levels of the communication system worry about it. Finally, if the system has high PMD, it needs to be actively mitigated.
7) *Study of PMD statistics and dynamics of installed fiber plant.* Unless PMD is so low that it can be ignored, it is obvious that the single most important piece of information, which is crucial to formulating outage probabilities, evaluating mitigation strategies, and developing compensation techniques, is the full understanding of *PMD dynamics*.

Existing theoretical tools and developments have been successful in predicting the statistical properties of an infinite ensemble of statistically equivalent fibers, and thus, a carrier might reliably estimate the number of transmission systems that can be expected to suffer an outage due to PMD. But the prediction of what will happen to a *particular* traffic-bearing field-installed fiber is a more difficult theoretical issue and also provides more valuable operational knowledge: is *this* fiber-optic transmission system (currently operational, creating revenue, and subject to service level agreements) likely to fail in the future, and if so, when and for how long? Much of the discussion to date has made implicit use of what might be called the "fast mixing assumption" that, from moment to moment, the fiber's state randomly samples the statistical ensemble and is equally likely to evolve into any of the other ensemble elements. In this view, the outage time per year would be calculated from the appropriate cumulative distribution function. While complete mixing undoubtedly occurs over long enough time scales, we will present evidence, gathered by groups on all continents, that the fast mixing assumption is generally not valid in field-installed (buried) fibers over practical time scales, and we will give an interpretation that has evolved over the last few years.

This paper is organized as follows: Section II contains an overview of birefringence and PMD, briefly reviews early field measurements, and introduces a "hinge" model for viewing such results. Since the model has slightly different emphases than the conventional model, this section's review is aimed at elucidating the terminology and concepts that we will use later in the text. Our development uses what has become the conventional notation [2]. The next two sections deal with long-term measurements of installed fibers that were not carrying live traffic, i.e., "dark" fibers. In Section III, we review our measurements of urban and suburban routes that were performed with the traditional interferometric technique and compare them to measurements by other groups. In the Appendix, we also discuss uncertainties in estimates of the magnitude of PMD associated with this technique and relate them to the nature of links composed of long stretches of buried fiber. Analysis of the measurement statistics gives evidence that fast mixing is not taking place. A more detailed measurement technique using wavelength-resolved measurements of dark fibers [7] gives greater insight into the dynamics of buried fibers and is discussed in Section IV. By comparing experimental PMD measurements with the ambient temperature, we show that it is

possible to establish upper bounds on the variability of buried sections of the fiber. While such dark fiber experiments are useful in developing an understanding of the underlying processes, deployed systems are much more complex. Section V deals with measurements on a live system. We discuss the consequences of optical components in offices and huts, as well as the presence of active components in the optical path, and describe them as another class of polarization-rotating "hinges." The last two sections describe how the experimental results developed in Sections III–V change the view of how outages arise and persist. In Section VI, temporal DGD statistics is reviewed, and the fact that outage probabilities can be expected to vary as a function of communication frequency is addressed. Finally, in Section VII, we explore several numerical and analytical approaches that might be taken to exploit the properties of these channel-specific outages. We conclude with open questions that might be addressed in future studies.

II. Background

A. Birefringence

The fundamental physical effect this paper is concerned with is the fact that imperfections and perturbations in fibers create polarization-dependent changes in the optical index of refraction. These are generally described as different indices of refraction (and hence different propagation velocities) for two distinct polarization eigenstates. The SOPs corresponding to these eigenstates are usually labeled "slow" and "fast": they are not generally the "x" and "y" polarizations but depend on the direction and nature of the perturbations that cause them. An arbitrary SOP can be resolved into components along the slow and fast eigenstates, and after propagating down a fiber of length L, these components will suffer a differential phase delay (due to differences in phase velocities v_p of the two eigenstates) of

$$\Delta\tau_p = \frac{L}{v_{ps}} - \frac{L}{v_{pf}} = \left[\frac{\beta_s - \beta_f}{\omega}\right] L = \frac{\beta}{\omega} L \qquad (1)$$

where the s and f subscripts denote the slow and fast eigenstates, respectively, and β is the difference between the two propagation constants. Since the SOP depends on the relative phase of the two components, it evolves as lightwave propagates. Information-bearing signals, however, have spectral content and travel at the group velocity. The DGD for a signal traversing the same birefringent medium, using the usual definition of group velocity, is

$$\Delta\tau_g = \frac{L}{v_{gs}} - \frac{L}{v_{gf}} = \left[\frac{\partial\beta_s}{\partial\omega} - \frac{\partial\beta_f}{\partial\omega}\right] L = \frac{\partial\beta}{\partial\omega} L = \beta' L. \qquad (2)$$

It is generally assumed that the group and phase velocities are similar, and their eigenstates are identical, arising from the physical perturbations.

The birefringence's magnitude and the orientation of its axes are generally not constant but vary randomly along the length of the fiber, which greatly complicates the above description for long telecom fibers. The most useful way to describe the situation is a geometrical representation based on the Poincare sphere. While the details [2], [8], [9] are beyond the scope of this paper, the basic representation is crucial and can be seen in outline form in Fig. 1. In short, a) each SOP is represented by a point (i.e., vector) on the Poincare sphere, b) the birefringence at a given fiber location is represented by a vector $\boldsymbol{\beta}$, pointing in the direction corresponding to the SOP of the slow eigenstate, and c) the SOPs rotate about the birefringence vector $\boldsymbol{\beta}$ at a rate equal to the magnitude of $\boldsymbol{\beta}$, namely β. Thus, the SOP rotates about a constant birefringence $\boldsymbol{\beta}$ by a total of βL radians in traversing a length L, regardless of the angle or "latitude" of the SOP with respect to $\boldsymbol{\beta}$.

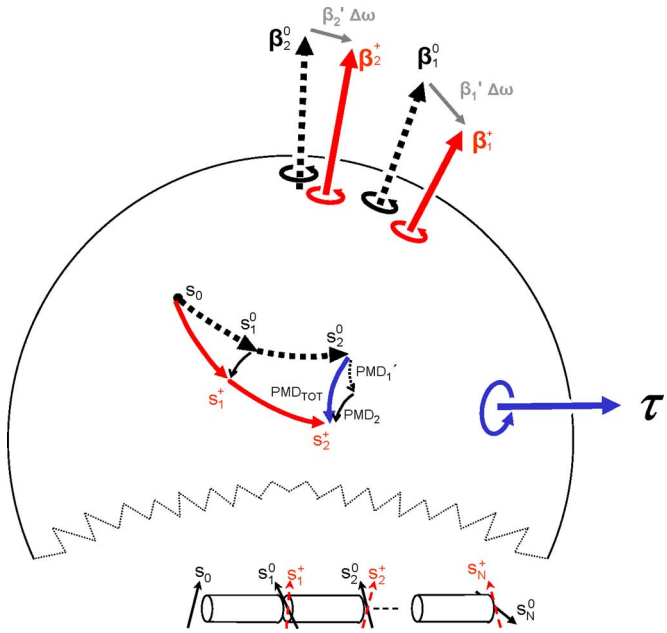

Fig. 1. Polarization evolution. Input polarization s_0 evolves in traversing two sections of birefringent fiber (lower inset). At ω^0, SOPs evolve on the Poincare sphere by sequentially rotating, with propagation distance, about dotted vectors $\boldsymbol{\beta_1^0}$ and $\boldsymbol{\beta_2^0}$, which represent the sections' birefringences. At frequency $\omega^0 + \Delta\omega$, SOPs evolve by rotating about solid vectors $\boldsymbol{\beta_1^+}$ and $\boldsymbol{\beta_2^+}$, where each are expressible as a first-order expansion (light arrows). The PMD viewpoint is that the output SOP for each section rotates about a PMD vector with changing frequency (light curves). Since each section's SOP is rotated by succeeding sections, the overall PMD vector is a concatenation of rotated section PMD vectors (see text).

Any actual fiber will have a $\boldsymbol{\beta}$ that varies with length, and this is shown schematically in Fig. 1 as a fiber with two sections (lower inset), with birefringences $\boldsymbol{\beta_1^0}$ and $\boldsymbol{\beta_2^0}$, represented by dotted arrows at the top of the Poincare sphere. (Here, superscripts denote frequency, and subscripts denote the section number, so $\boldsymbol{\beta_1^0}$ represents the birefringence vector of section "1" at optical frequency ω^0.) In traversing "section 1," an initial SOP of $\mathbf{s_0}$ at frequency ω^0 rotates $\beta_1 L$ radians about $\boldsymbol{\beta_1^0}$ to SOP $\mathbf{s_1^0}$ followed by a rotation of $\beta_2 L$ radians about $\boldsymbol{\beta_2^0}$ to SOP $\mathbf{s_2^0}$. Further sections would continue the rotations, and a general optical fiber might be considered as a concatenation of such birefringent sections. This "retarder plate" model of a fiber is the most commonly used model for fibers. The lower inset in Fig. 1 shows the fiber as constructed of a series of retarder plates, each with its own birefringence, causing the polarization at each frequency to evolve as it propagates down the fiber.

B. PMD

In contrast to the monochromatic (i.e., at frequency ω^0) case, PMD is concerned with the behavior of signals that have finite spectral content. Consider a component of the optical signal at a nearby optical frequency $\omega^0 + \Delta\omega$. This component experiences birefringences that are slightly different (solid arrows, $\boldsymbol{\beta}_1^+$ and $\boldsymbol{\beta}_2^+$); therefore, this light (although launched in the same SOP) will travel on slightly different arcs to $\mathbf{s}_1^+$ and $\mathbf{s}_2^+$ under the influences of these new $\boldsymbol{\beta}$ vectors. Since we assume that $\Delta\omega$ is small compared to ω_0, $\boldsymbol{\beta}_1^+$ can be expressed as a first-order expansion $\boldsymbol{\beta}_1^+ = \boldsymbol{\beta}_1^0 + \boldsymbol{\beta}_1'\Delta\omega$, and similarly for $\boldsymbol{\beta}_2^+$ (gray arrows in Fig. 1). In examining the SOP evolution under $\boldsymbol{\beta}_1^+$, we see that $\mathbf{s}_1^+$ can be viewed as an additional rotation of $\mathbf{s}_1^0$ by $(\beta_1'\Delta\omega)L$ about vector $\boldsymbol{\beta}_1'\Delta\omega$, taking $\mathbf{s}_1^0$ to $\mathbf{s}_1^+$ (light curve) since it is a differential rotation. But the same rotation can *also* be viewed as a rotation of $(\boldsymbol{\beta}_1' L)\Delta\omega$. This latter form is the definition of PMD. We say that $\boldsymbol{\tau_1} = \boldsymbol{\beta}_1' L$ is the PMD for section 1, that the magnitude $|\tau_1| = \beta_1' L$ is the DGD for section 1 (see eq. 2), and that the SOP moves on the Poincare sphere by an angle of $|\tau_1|\Delta\omega$ for a frequency offset of $\Delta\omega$. The same thing occurs for section 2, although now we are operating on $\mathbf{s}_1^+$, which can be considered at the sum of two arcs: one from $\mathbf{s_0}$ to $\mathbf{s}_1^0$, and one from $\mathbf{s}_1^0$ to $\mathbf{s}_1^+$.

This figure illustrates all the essential points needed for our discussion of PMD. 1) Each section has its own PMD, shown as gray arcs generated by rotations about $\boldsymbol{\beta}_1' L$ and $\boldsymbol{\beta}_2' L$ (corresponding to $\boldsymbol{\tau_1}$ and $\boldsymbol{\tau_2}$). These generate rotations for output SOPs as the optical frequency is changed. 2) The net effect of changing the optical frequency, when viewed at the final output of section 2, is that the SOP is rotated about some "other" axis, represented by vector $\boldsymbol{\tau}$ on the right. This is the PMD for the entire link since it describes how the polarization disperses with optical frequency. 3) The PMD $\boldsymbol{\tau}$ is not the vector sum of $\boldsymbol{\tau_1}$ and $\boldsymbol{\tau_2}$ because the rotation done by $\boldsymbol{\tau_1}$ occurs at a different orientation than the rotation done by $\boldsymbol{\tau_2}$: there was an intervening rotation by $\boldsymbol{\beta}_2^0 L$. That is, when $\boldsymbol{\tau_2}$ rotates $\mathbf{s}_1^+$, it can be viewed as simultaneously rotating $\mathbf{s}_1^0$ and the gray arc (generated by $\boldsymbol{\tau_1}$) connecting $\mathbf{s}_1^0$ and $\mathbf{s}_1^+$. This "imaged" arc, labeled as PMD_1', can be viewed as having been caused by a version of $\boldsymbol{\tau_1}$ that is imaged by the same rotation. This is the source of the concatenation rule [3] and is responsible for much of the richness of the PMD properties: each section's PMD vector is rotated by all sections following it, creating an image PMD at the output. The sum of these *imaged* PMDs is the total PMD.

The formal mathematical description of the arguments above, when the sections are reduced to infinitesimals, is the set of dynamical equations first proposed by Poole *et al.* [10], expressed in conventional form as

$$\frac{\partial \vec{s}}{\partial z} = \vec{\beta} \times \vec{s} \tag{3}$$

$$\frac{\partial \vec{s}}{\partial \omega} = \vec{\tau} \times \vec{s} \tag{4}$$

$$\frac{\partial \vec{\tau}}{\partial z} = \vec{\beta}' + \vec{\beta} \times \vec{\tau}. \tag{5}$$

In words, the first equation states that $\boldsymbol{\beta}$, the phase velocity birefringence, rotates the SOP (at a fixed frequency) as a function of distance. The second equation states that the PMD rotates the SOP (at a fixed distance) as a function of frequency. The third equation states that the PMD grows, as one moves down the fiber through a small section, by rotating the existing PMD about $\boldsymbol{\beta}$ of that section and adding the section's PMD $\boldsymbol{\beta}'\Delta z$ to the result, as described above.

C. Statistics of PMD

From the early work of Curti *et al.* [11] and Foschini and Poole [12] to recent times, the analogy of the random driving term above $(\boldsymbol{\beta}')$ to Brownian motion has been exploited as a set of stochastic differential equations (SDE) to glean the statistical properties of the total PMD vector. The "white noise" spectrum requires special mathematical approaches but results in relatively simple differential equations to solve. By its nature, the SDE approach is more suited for treating uniform systems. With the model developed above, however, we can represent more varied situations, such as inhomogeneous statistics for birefringence, we can describe the potential for PMD vectors to evolve continually in time, and we can also investigate some of the statistical properties. For instance, we saw above that the fiber's PMD vector is the sum of each fiber section's PMD vectors after each of them has been imaged all the way down the end of the fiber. This problem is, in fact, identical to that of a classical gas in which molecules have random velocities, and therefore, we can appropriate the result that the net distribution for the mean length of the PMD vector (the DGD) has a Maxwellian distribution.

The model also suggests a view of how the PMDs at neighboring frequencies are related, i.e., the spectral autocorrelation of the PMD. If the PMD for each section is large enough, or if the frequency spread is large enough, each section's image at the output will be totally uncorrelated with the image at the original frequency. However, although the two PMDs are uncorrelated, they still will be drawn from the same Maxwellian distribution. This shows that if one samples over a wide enough optical bandwidth, it is essentially equivalent to picking another element from the ensemble, and the situation will look like the "fast mixing" assumption. On the other hand, if the statistics are not Maxwellian, it is an indication that only a restricted set of the ensemble is being sampled.

Another application we will use is the idea that the retarder plates may be nonuniform: One plate may have a much greater PMD than the others. Simple geometric arguments show us that the total PMD will be dominated by this vector, which is a point to which we will return in later sections.

D. Field Measurements

As mentioned above, PMD can be expected to change in time. The sources of these changes are variations in the magnitude or orientation of the birefringences (and hence the section PMDs) over time, and perturbations such as temperature, pressure, stress, cabling orientation, bending, relaxation, aging, etc., are all expected to make changes in the PMD. Environmental sensitivity was recognized very early when Poole *et al.* first noticed a temporal DGD drift in laboratory spools [13], and then

observed related transmission power penalties [14]. At about the same time, De Angelis *et al.* observed large changes in signal SOP in buried terrestrial links, in which some fiber connectors were contained in cabinets placed above ground [15]. These changes occurred at sunrise and sunset and were ascribed to abrupt changes in ambient temperature. Thus, the environmental sensitivity of long links has been established since the earliest days of PMD.

As the deployment of 10- and 40-Gb/s systems was anticipated in the late 1990s, many field experiments were performed [16]–[24]. Most of these were focused on determining the PMD's rate of change in installed routes, presumably to ascertain how long an operating link might be expected to remain viable. The results reported by different groups varied dramatically, but all of them indicated that the PMD variations in installed cables are rather slow. These variations occurred on time scales ranging from a few hours to several days. Such a large spread suggested that the particular details of the cable installation must play a significant role in PMD dynamics. This further motivated a search for a unifying model that would describe the PMD temporal dynamics of any fiber route.

At the other end of the time scale, investigations into potential sources of very rapid fluctuations also proceeded since many rights of way were under or near heavily used transportation routes that were expected to subject the fibers to vibrations. Several experiments looked for fast (millisecond scale) PMD variations [22], [25]–[28]. While fast events do indeed occur in installed fibers, they are generally solitary, isolated in time, and very rare. Up to date, the consensus in the industry is that fast events most likely originate from human activities in the offices.

E. Hinge Model

As a carrier, AT&T has long been interested in understanding the fundamentals of PMD on long routes, and in this paper, we will review several experimental efforts that have been undertaken both in AT&T and outside in the last four to five years with a focus on gaining insight into the polarization dynamics of installed fiber routes. We will show evidence suggesting that most of the temporal changes in PMD that have been observed in installed routes arise primarily from a relatively small number of "hot spots" along the route that are exposed to the environment. On the other hand, the long buried sections that make up the bulk of the link length remain largely stable for periods on the order of weeks to a month. Hourly and daily environmental changes cause fiber in the hot spots to change in birefringence and thus to act as time-dependent polarization rotators. The general picture, then, is that a long link is considered to be a large, but finite, set of concatenated fiber sections (retarder plates, as in the inset to Fig. 1). While each of the retarder plates has a random birefringence, for the most part, they are fixed in time due to the stable environment they experience in their buried conduits. At a few places (bridges, etc.), the conduits are not buried but are exposed to ambient temperature. These sections can change their birefringence in time. When viewed at the output, the fiber's PMD is then composed of a relatively small number of large stable PMD vectors (the buried sections) that suffer, in addition to the stable rotations by succeeding buried sections, time-varying rotations from the hot spot sections. These time-varying rotations can be thought of as hinges that add a time-dependent component to the images of the longer stable sections. As such, instead of the conventional retarder plate model of a long fiber link, a more apt mode, at least in terms of its time evolution, would be as a few-section PMD emulator. This is the essence of our hinge model [29]. The major statistical implication of our empirical hinge model is that the temporal statistics of PMD becomes channel specific, thus requiring a new perspective on PMD-driven system outages.

Armed with this background, we are in a position to review the existing experimental data for long-term issues in PMD.

III. Long-Term Measurements of Spectrally Averaged DGD on Dark Buried Fibers

An interferometric PMD measurement technique [30] permits one to obtain a frequency average of fiber DGD values in a single quick scan. Relative ease of use and a variety of available commercial instruments made it the carriers' technique of choice for routine PMD characterization of their installed fiber plants. The widely accepted metric for the PMD of the fibers is the value of the rms DGD averaged over an *infinitely* large frequency range, namely $\tau_{\rm rms}$.

It turns out that this parameter $\tau_{\rm rms}$ cannot be measured precisely for recent vintage ultralow DGD fibers. The problem is not fundamental but rather technological. Experimentally, $\tau_{\rm rms}$ is approximated by $\tau^B_{\rm rms}$, namely the rms DGD when averaged over a *finite* bandwidth B. The resulting *rms* DGD $\tau^B_{\rm rms}$ is a stochastic variable itself with known distribution and standard deviation, analytically expressed for sufficiently large B as $\sigma \propto \sqrt{\tau_{\rm rms}/B}$ [31], [32]. The lower the $\tau_{\rm rms}$ of a fiber, the wider is the bandwidth of its DGD frequency autocorrelation function [32], [33], and thus the wider is the bandwidth needed to sample all possible values of τ. Therefore, a wider frequency range B is needed for $\tau^B_{\rm rms}$ to be an accurate estimate of the mean DGD value $\tau_{\rm rms}$ of low-PMD fibers. With current commercial light sources having a spectrum of no more than 100 nm, a measured mean DGD value $\tau^B_{\rm rms}$ of 0.2 ps (which corresponds to a 100-km link of a 0.02-ps/km$^{1/2}$ fiber) approximates the true value $\tau_{\rm rms}$ with a 100% error! The aggregate errors for multispan routes are addressed in Appendix.

However, because the quantity $\tau^B_{\rm rms}$ is not a unique fiber constant, it can be used to monitor the stability of installed fibers over time. If the fiber under test is exposed to a time-varying environment (as for installed cables), the details of the fiber DGD frequency spectrum $\tau(f)$ change in time, which, in turn, is likely to cause observable changes in $\tau^B_{\rm rms}$ since it is a sample over a finite region of the spectrum.

In 2002, long-term field measurements of $\tau^B_{\rm rms}$ were performed on multiple fiber strands in three different AT&T routes [34], [35]. Two were suburban ones laid out along a major highway, about 80 km each. The third route, which is 7 km long, was located in a major city. The measured fiber strands were a mixture of single-mode and TrueWaveRS fibers and belonged to different ribbons. Data were continuously taken for several days in the months of February and August of 2002.

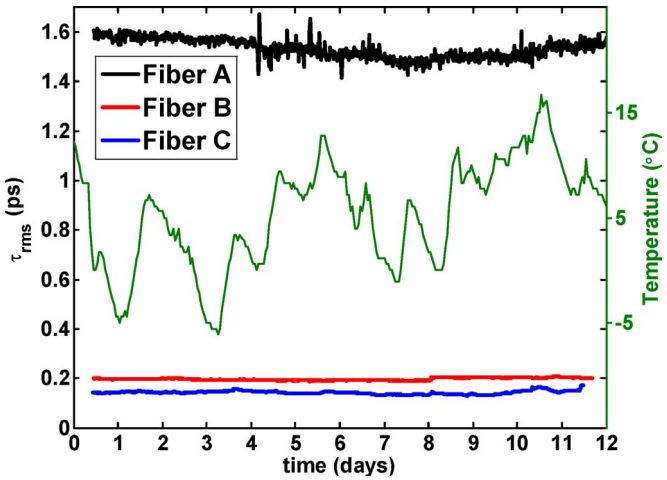

Fig. 2. Measured rms DGD $\tau^B_{\rm rms}$ for three completely buried city fibers (thick lines). The data are independent of the ambient temperature (thin green line, right axis).

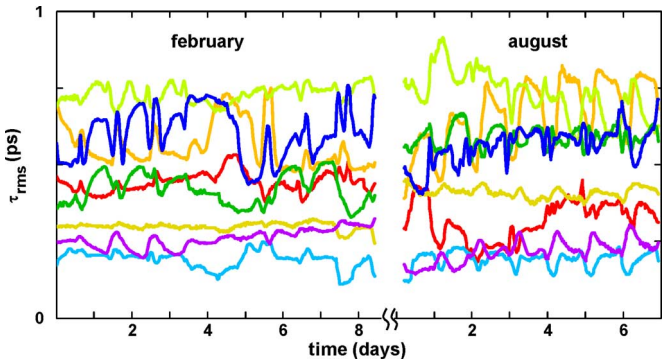

Fig. 3. RMS DGD $\tau^B_{\rm rms}$ for eight fibers in a suburban buried cable. The data span nine days in February and seven days in August. Strong daily variations are evident from the data.

Fig. 2 shows the values of mean DGD for three city fibers continuously measured together with the simultaneously measured ambient temperature. As temperature evolved with time, almost no change in $\tau^B_{\rm rms}$ was observed for this link, which was a fully buried underground. On the other hand, the two suburban links with a few sections exposed to temperature variations (such as tens of meters long bridge attachments) show small and largely reversible variations in mean DGD estimates, which track the ambient temperature. The left side of Fig. 3 shows values of $\tau^B_{\rm rms}$ for eight fibers in the same cable measured in February, and the right side of Fig. 3 shows data for the same fibers obtained half a year later (the temperature, which was also measured is not shown). The exact functional dependence on temperature varies from one fiber strand to another [34], [36] and might not be very informative because the measured data represent a spectral average. However, the mere *presence* of diurnal shifts occurring only on fibers with exposed sections suggests the major role these short sections play in the rather complex PMD temporal dynamics. This conclusion is in accord with results from other groups on various routes across the globe [15], [21], [36]–[39].

A related but more important conjecture follows from data on the long-term stability of completely buried parts [35]. Indeed, these diurnal fluctuations are small in amplitude and occur around the same level even when measured half a year later for six fibers in Fig. 3, whereas for two fibers, the levels shifted just slightly. The resulting distributions of $\tau^B_{\rm rms}$ taken at different times deviate strongly from the Gaussian shape predicted by the central limit theorem and are much narrower than the theoretical value [31], [32]. These discrepancies indicate that for each fiber, the set of measured values $\{\tau^B_{\rm rms}\}$ represent only a minor portion of the entire ensemble of all possible states of that fiber. In other words, fibers are not sufficiently scrambled, apparently due to the time stability of our buried links. This suggests that mixing is taking place slowly on these time scales.

IV. Wavelength-Resolved Long-Term DGD Monitoring Experiments on Dark Fibers

A. Experimental Data

Further insight into the long-term stability of dark fibers can be gained from the month-long spectral PMD measurement on installed fiber [40], [41]. By employing the Müller matrix method [7] with optical preamplification, this experiment encompassed a wide optical band (100 nm) and long reach (160 km). The measurement equipment was collocated, and the link was looped back, consisting of two fibers described in the previous section and shown in Fig. 3. These were predominantly buried fibers: several sections, such as bridge attachments tens of meters long, were left vulnerable to environmental changes.

Daily local ambient temperature changes of about 10 °C were reflected in the DGD spectra, causing DGD changes for each wavelength. For some wavelengths, the changes were relatively large (about 0.5 ps compared with mean DGD of 0.64 ps), whereas for others, they were small. The overall spectrum appears to be "breathing" with temperature: peaks and valleys change their levels while remaining at the same wavelength [41]. In our laboratory, we observe much a simpler behavior (a shift of the total spectrum in wavelength with temperature) on spooled fiber of the same type, i.e., when the entire fiber is immersed in a time-varying temperature bath. Interestingly, such a shift can be explained in terms of phase conservation of the lightwave: the phase of the lightwave, which controls the polarization properties, is related to the ratio of the optical path to the wavelength, i.e., $\phi \approx nL/\lambda$, where n is the refractive index, and L is the physical length [42]. Inside the thermal bath, the optical path nL changes uniformly along each section of the fiber length, and this change (when sufficiently small) can be compensated by corresponding adjustments in λ. Thus, spectral breathing being different from spectral shift is indicative of the nonuniformity of the applied temperature in the field fibers.

Surprisingly, the DGD spectral changes were largely reversible. That is, when at some later time the temperature returned to a previous value, the DGD also returned to its previous value. In other words, by viewing the DGD at any given wavelength as a function of temperature alone, one can account for most of the variations observed. Two DGD spectra taken 15 days *apart* but at the *same* temperature look surprisingly alike despite large changes, in the interim, in both T and DGD (Fig. 4). Such a comparison of full DGD spectra conditioned on temperature, which was made for the first time in [40] and [41], separates the temperature-driven variations caused

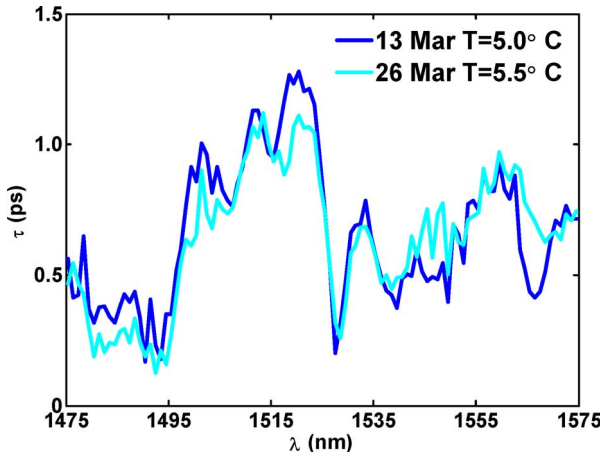

Fig. 4. Two DGD spectra taken two weeks apart but with the same temperature on a buried cable with several exposed parts. Note the similarity in spectral features despite large changes happened in the interim.

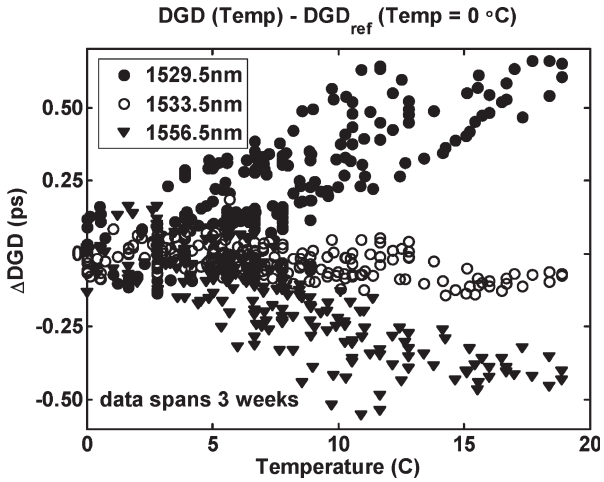

Fig. 5. Changes in DGD for three wavelengths $\lambda = 1529.5$ nm (•), 1533.5 nm (○), and 1556.5 nm (▼) presented as a function of time. The data span over three weeks of measurements. A reference point $\mathrm{DGD}_{\mathrm{ref}}(\lambda)$ is chosen at $T = 0\ ^{\circ}\mathrm{C}$. From [41].

by the exposed parts from the underlying slowly varying long-term structure of DGD spectra, which is presumably related to changes in buried parts of the fiber.

This idea can be further illustrated by plotting the deviations in DGD for several wavelengths: $\Delta\mathrm{DGD}(\lambda_i) = \mathrm{DGD}(\lambda_i) - \mathrm{DGD}_{\mathrm{ref}}(\lambda_i)$ not as a function of time but of temperature (Fig. 5). Here, a reference value $\mathrm{DGD}_{\mathrm{ref}}(\lambda_i)$ is chosen at one point in time, when the temperature was 0 °C. The data sets span a time period of 21 days. An *unexpected* monotonic functional dependence with temperature can be clearly seen for each wavelength. The scatter of the data, which tend to increase for data sets covering a longer time span [41], suggests an increasing influence of the slow irreversible changes in the fiber system, which apparently occur on a time scale comparable to a month.

B. Quantitative Analysis

To quantify these irreversible variations in DGD and to separate them from the functional DGD dependence on temperature,

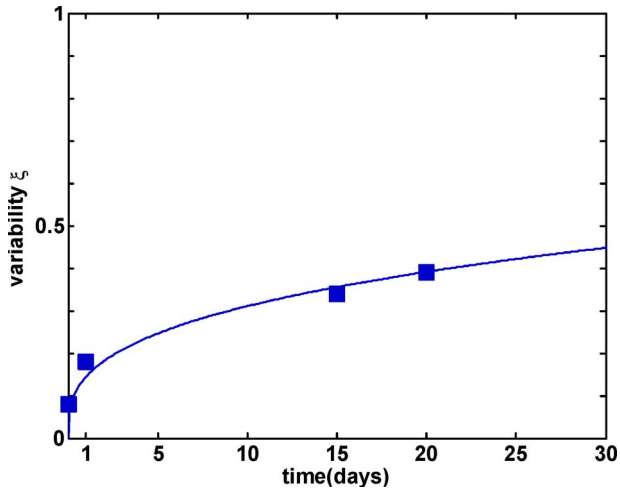

Fig. 6. Variability ξ as a function of time (squares). ξ is the average deviation that the DGD at any given wavelength experiences, normalized to the mean DGD. Thin line is a guide to the eye.

we introduce the "variability" metric

$$\xi(t, t_0) = \frac{\sqrt{\langle(\tau(\lambda, t) - \tau(\lambda, t_0))^2\rangle_\lambda}}{\sqrt{(3\pi - 8)/4} \times \langle\tau\rangle}. \tag{6}$$

It is the rms difference between two $\mathrm{DGD}(\lambda)$ spectra taken at times t and t_0 normalized so that $\xi = 0$ for two identical spectra and $\xi = 1$ for two completely decorrelated spectra with the same mean $\langle\tau\rangle$. We note that ξ can be viewed as the average deviation that the DGD at any given wavelength experiences, normalized to the mean DGD. The averaged variability computed for spectra conditioned on the *same* temperature is shown schematically in Fig. 6. For the DGD spectra taken *at the same temperature* but as many as 20 days apart, the variability is only $\xi = 0.39$. In contrast, daily excursions of the temperature could cause variabilities of up to $\xi = 0.89$.

A similar correlation analysis was proposed by the Telecom Italia team [37]. By assuming a periodic temperature, the authors compared DGD spectra taken 24 h apart. The results of both experiments are in qualitative agreement, but the Telecom Italia fiber showed faster decorrelation. The metric $R(t)$ used in [37] is related to the variability ξ by the simple relation $R(T) = 1 - \xi^2$. Thus, the reported R value for time separation of seven days of 0.1 is equivalent to a ξ of 0.95. The ambiguity in the temperature (i.e., a temperature measurement might have revealed variations that were not perfectly periodic) might have caused the seemingly faster decorrelation.

To summarize, the observed spectral evolution was ascribed to the fact that only *a few* sections, tens of meters long and located over the length of the link, are exposed to ambient temperature variations. A possible explanation of how changes of a very short (relative to the total route length) section could result in rather large changes in DGD is the hypothesis that these sections act as polarization rotators [37], [40], [41]. Indeed, when only one fiber section keeps changing while the rest are constant, the concatenation rule reduces to a summation of two vectors connected by a hinge. The movement of only

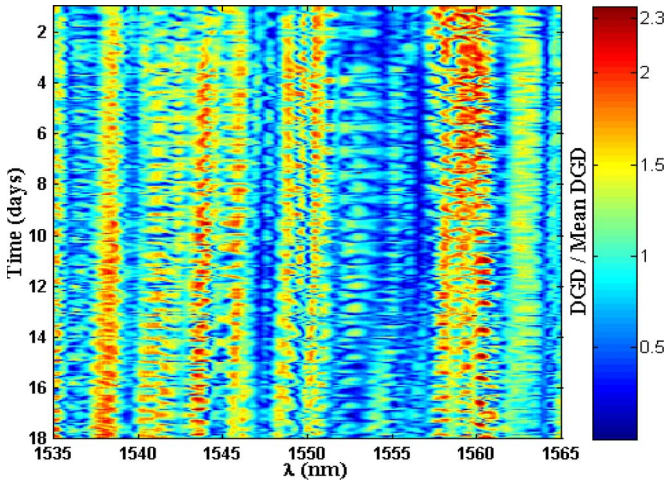

Fig. 7. Experimental DGD (normalized to its mean value) as a function of wavelength and time (vertical axis) for the link comprised of two buried fibers connected in a hut via an EDFA. From [44].

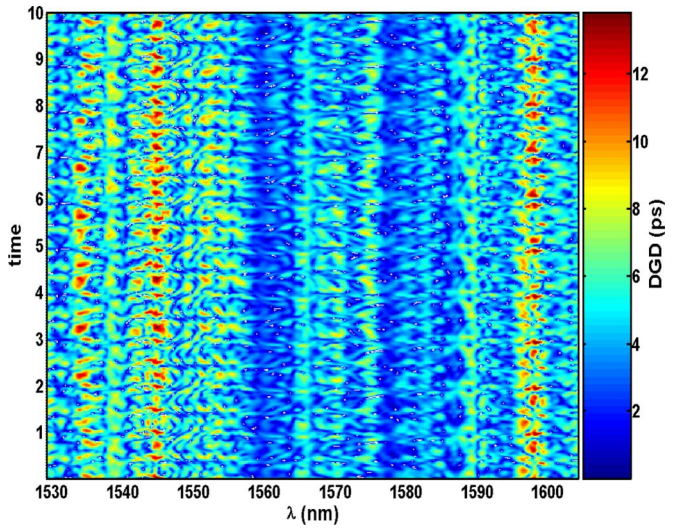

Fig. 8. Numerical DGD as a function of wavelength and time (vertical axis) for a link with four hinges. Note the quasi-periodicity and spectral persistence of high and low DGD events similar to that of the data in Fig. 7.

one hinge can cause large changes in DGD, especially if the hinge is located near the middle of the fiber. Later simulations confirmed that a reversible SOP rotator with amplitude (in the Stokes space) of only $\pi/3$ radians can result in DGD changes of the magnitude observed [43]. On the other hand, the observed reversibility suggests two things: first, that the hinges seem to be somewhat, if not completely, reversible, and second, that the buried sections are largely stable. In other words, even if the increase in ξ is attributed solely to the buried parts (assuming a complete reversibility of ideal hinges with ambient temperature changes that are uniform over the link), an observed decorrelation of the entire fiber on a month-long scale serves as a lower bound on the decorrelation time scale of the buried parts.

C. Manifestation of the Hinges

The way hinges manifest themselves in field PMD data depends on many factors, such as their number, driving forces, and the scope of rotation. Two illustrative examples are given in Figs. 7 and 8. Here, instantaneous DGD values are represented by color as a function of wavelength and time, with the warmer color corresponding to higher values. Fig. 7 presents 18 days worth of experimental data obtained by Kondamuri *et al.* [44] on the concatenation of two Sprint fiber spans (95 km each) joined via an erbium-doped fiber amplifier (EDFA). The same authors report rapid variations in DGD compared to that observed on individual fibers [45] and spectral localization of high-DGD events. Both features are evident on the plot. Although the cause of variation was not reported in [44], we suspect they arise from several hinges along the route. To investigate this hypothesis we performed a rather straightforward hinge modeling, results of which, presented in Fig. 8, are seemingly similar to the real data shown in Fig. 7. Five stable fiber spans, each consisting of 200 randomly birefringent sections, were connected by four hinges [43]. Hinges were modeled as Stokes-space rotators about fixed frequency-independent axes whose angle of rotation α evolved as a predetermined function of time: $\alpha_k = 1.5\pi \sin[2\pi f t + (k-1)\pi/8] + 2\pi t/500$, where $f = 1/50$, where k is the hinge number. Quasi-periodicity in time and spectral persistence of both high and low DGD event relate Fig. 8 to Fig. 7.

V. PMD Experiments on Field-Deployed Telecom System

The PMD penalties in a fiber-optic communication system are not exclusively controlled by the PMD of the fiber itself and its dynamics. Various system components, which are regularly placed along the link, such as optical amplifiers and dispersion compensation modules (DCMs), may also play an important role in determining both the output SOP and the temporal dynamics of the system PMD. Here, we describe an experiment focused on elucidating the effect of repeaters and their equipment. A commercial ultralong-haul Raman-amplified 40-Gb/s system, which is comprised of six spans, was installed between two major cities [46]. The two end terminals (T1, T2) were placed in switching offices in the cities, and five repeaters (R1–R5) were installed in small unmanned buildings, with R3 collocated with R1. (Note that our use of the term "repeater" is something of an anachronism: these sites contain optical amplifier equipment.) Span lengths ranged from 43 to 111 km, and the total T1–T2 distance was 493 km. For the tests described below and reported in detail [29], [47]–[52], three different configurations looped back to T1 from R1, R3, and T2 were used, with corresponding transmission distances of 222, 562, and 986 km, respectively. For long-term PMD monitoring, a tunable probe laser with a controlled SOP was injected via a coupler onto T1's "transmit" fiber, and a polarimeter was used to measure the returning light tapped from T1's "receive" fiber. The usual data traffic was disabled so only the probe was present through the amplified media. Again, the Müller matrix method was utilized. In a separate experiment, Boroditsky *et al.* devised an original *in situ* technique to measure PMD using a "live" data-carrying channel, thereby not only obviating the need for a probe laser but also establishing a correlation between the time-varying PMD and the quality of transmission [51], [52].

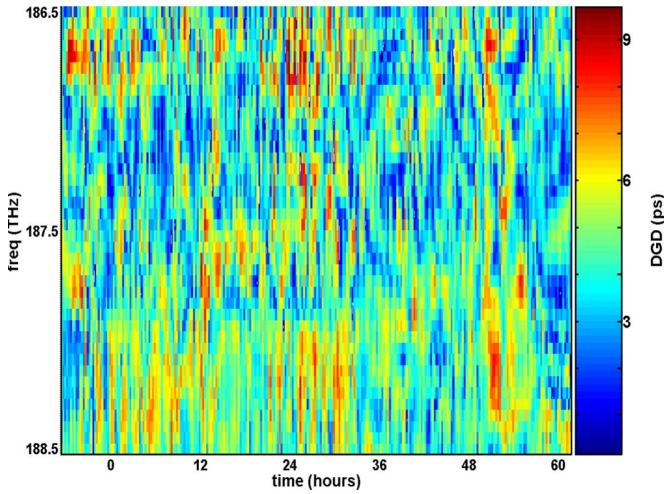

Fig. 9. Colorplot of the DGD spectral evolution in time (horizontal axis) measured through a field-installed 986-km Raman-amplified system.

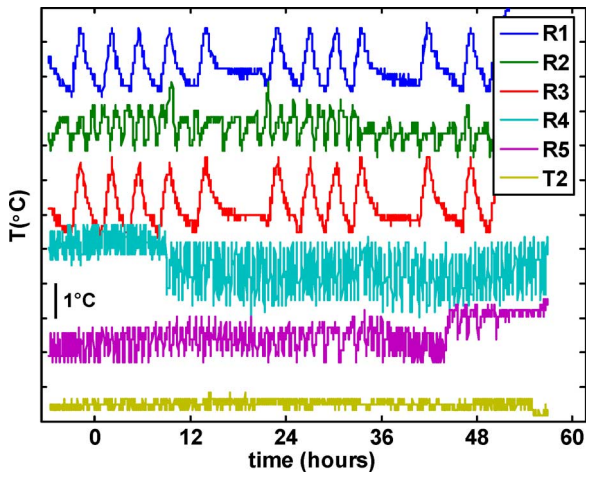

Fig. 10. Equipment temperature in the optical amplifier's sites measured concurrently with the data in Fig. 9. The data are shifted for clarity. Vertical scale is indicated by 1 °C bar.

The temporal evolution of the DGD spectrum of the full 986 km is shown as a colorplot in Fig. 9. The most surprising features are the fast (< 1 h) and dramatic variations of the DGD of the system. Since these were too fast to arise from outdoor temperature effects, we investigated the temperatures inside the buildings that house the equipment and found that they changed on a similar time scale. While each building interior is temperature controlled with a conventional thermostat, the latter has a hysteresis band of about 1 °C. Thus, small (1 °C to 1.5 °C) and periodic (1–3 h) temperature variations are to be anticipated. Fig. 10 shows the temperature inside all repeater sites as well as inside T2. Note the relatively large magnitude of temperature fluctuations at remote locations R1 and R3 compared to the high temperature stability at the city office, which is located in a well air-conditioned building. While the DGD spectrum shows a seemingly visual correlation with the temperature fluctuations in Fig. 10, the different temporal characteristics of temperature at various locations do not give rise to a statistically significant correlation coefficient. Nevertheless, the apparent dependence of the DGD spectrum on repeater temperature prompted us to

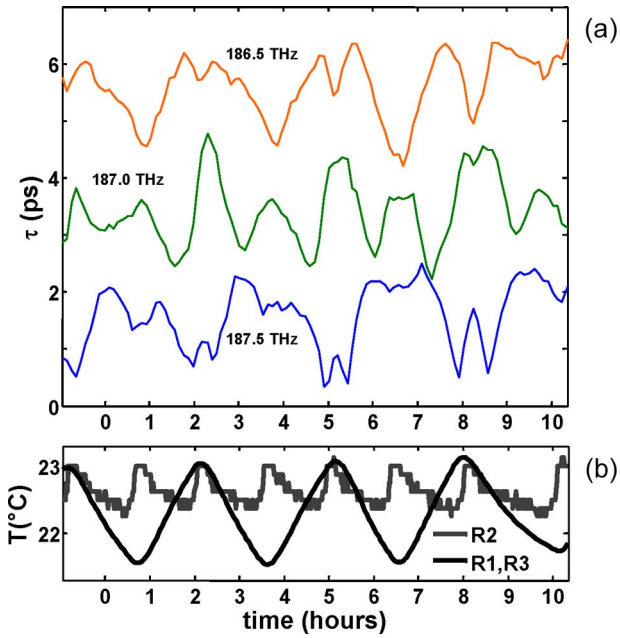

Fig. 11. (a) DGD for three optical frequencies 187.5 THz (blue), 187.0 THz (green), and 186.5 THz (orange) measured on shorter 562-km field deployed system. (b) Equipment temperature in two locations along the route.

carry out a controlled heating experiment in the hut housing R1 and R3. Every repeater in our system contained a dispersion compensation module (DCM) – a packaged spool of negative chromatic dispersion fiber chosen to match the positive dispersion of the transmission fiber. We heated the DCMs in the hut one by one and simultaneously monitored the DGD spectrum at the T1 terminal. Indeed, abrupt heating gave rise to a slightly delayed but rapid change in the DGD spectrum. Moreover, heating of the other parts of the system did not seem to produce any effect. Additionally, we verified in a separate laboratory test that the DCMs acted as strong polarization rotators in response to heating by 1 °C to 2 °C. We thus conclude that the DCMs are temperature-dependent polarization rotators producing large rotations for temperature fluctuations of the order of ~ 1 °C. Such characteristics make the DCM an excellent candidate for being a temperature-controlled hinge.

Fig. 11 presents the recorded temporal variations of the system's DGD spectra for three optical frequencies, acquired over a shorter 562-km route. To reduce the number of possible hinges, the system was shortened by looping at the third repeater, resulting in a T1–R1–R2–R3–R2–R1–T1 configuration. Also, a different lower PMD fiber strand from the same cable was used in this configuration. Note that the hut housing R1 and R3 not only shows the strongest and most distinct temperature oscillations, but unlike the other huts, this one happened to house two repeaters, so the signal passed through it four times, magnifying the effect of temperature variations. By reducing the number of hinges, nearly all features in the spectrum can be quite clearly traced to the temperature variations in the two remaining huts, which are shown at the bottom of the figure. These observations lead us to generalize the hinge picture to include not only bridges but also in-line components, which, like bridges, are discretely distributed along the link and are exposed to temperature or other environmental effects.

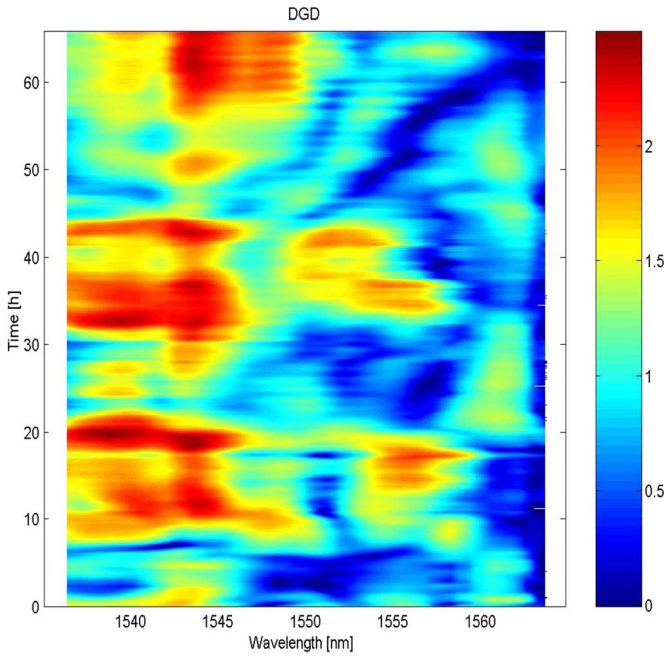

Fig. 12. Long-term DGD measurement for an amplified link with periodic spans and equal PMD of spans. Note some diurnal repeatability together with smaller and faster oscillations, most clearly seen at 1553 nm around the 60-h mark. From [54].

Several experiments on PMD dynamics in installed European links support our hinge model. For example, Weiershausen *et al.* report drastic differences in polarization dynamics originating from buried links and DCMs [53]. More recently, Leppla *et al.* report similar PMD dynamics observed on links in three routes in Germany and France [54]. The DGD data from one of the links are plotted in Fig. 12. The authors of [54] attribute the periodicity seen on the color panel to temperature-driven reversible hinges.

A. Long-Term Lab Study of Polarization Rotation by a DCM

A more detailed long-term laboratory study of the polarization rotation caused by a DCM subjected to small daily temperature fluctuations of the type expected in large telecommunication offices was conducted by Brodsky *et al.* [55]. For nine months, frequency-dependent polarization transfer matrices and the temperature of a DCM were simultaneously measured. The DCM was placed in a room with conventional temperature-regulation: benign conditions similar to that of a field office. Fig. 13 depicts output SOP traces on the Poincare sphere for three optical frequencies with a fixed input polarization. The observed polarization rotation had different characteristics on short and long timescales. On small timescales of about five to ten temperature peaks (usually 0.6 °C–1 °C amplitude peaks were occurring each 12–24 h), the DCM had a practically repeatable and reversible response, rotating the input polarization back and forth by any number between 0° and 180° on the Poincare sphere depending on optical frequency and time. However, on longer time scales, an additional random component is added to the rotation, which does not seem to be related to the observed temperature changes. At random times, either the angle or the direction of rotation or both could drift

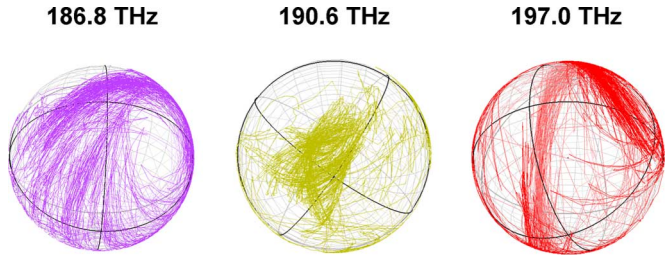

Fig. 13. Polarization evolution by a DCM. Output SOP traces as a function of time for fixed input SOP are presented on the Poincare sphere for three typical frequencies. Each sphere shows nine months of continuous data.

significantly in a relatively abrupt fashion, starting a significantly different output SOP trace on the sphere. Autocorrelation analysis determined the average time between these shifts to be about 30 days.

VI. Statistical Implication of the Hinge Model

DGD temporal statistics is important because engineering rules governing a system's test and deployment procedure rely heavily on it. It is often believed that the scrambling of DGD spectra over time leads to frequency-independent statistics for any given channel. In other words, the DGD at any given frequency is believed to sample the *same* Maxwellian distribution with the *same* mean value τ_{mean}. The validity of this assumption rests on a model in which dozens to hundreds of birefringent fiber sections undergo random reorientations over timescales of interests.

However, if DGD dynamics depends only on a small number of hinges, as we expect for field-installed fibers, we would expect the DGD statistics for those fibers to be different. Indeed, one may view the PMD vector *at each frequency* to be made of several fixed-length vectors (representing "dead" buried sections) connected by active hinges. These fixed vectors are larger at some frequencies and smaller at others. Therefore, for each frequency, the resulting DGD is the magnitude of the vector sum of the randomly oriented vectors, each of fixed length. Then, over the timescales for which the buried fiber can be considered "dead" [21], [23], [24], [41], gyrating hinges produce a distribution of DGD values that, for each individual frequency, is similar to that of a typical fixed-section PMD emulator. However, in contrast to typical emulators, the frequency-dependent lengths of the individual sections result in frequency-dependent mean DGD values $\langle\tau_{\mathrm{ch}}\rangle_{\mathrm{time}}$.

Brodsky *et al.* presented a statistical analysis of the data described in Section IV [49], [50]. Interestingly, as DGD spectra change over time, some spectral variations remain: some channels were observed, on the average, to experience a mean DGD almost twice as high as others. That is, as the DGD for a given channel varies in time, it constitutes a distinct statistical distribution dependent on the magnitude of the PMD for the stable sections at that channel's optical frequency, so that the mean value $\langle\tau_{\mathrm{ch}}\rangle_{\mathrm{time}}$ is channel specific and can differ among channels by a factor of about 2. Also, the standard deviation of the distribution sampled by each channel σ_{ch} was found to be frequency dependent as well. It seems to be higher for larger values of $\langle\tau_{\mathrm{ch}}\rangle_{\mathrm{time}}$.

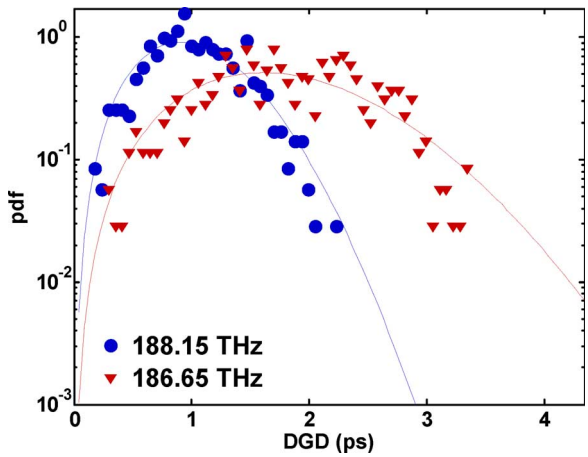

Fig. 14. Experimental DGD probability density of observations (symbols). Thin lines are guides to the eye. From [50].

Fig. 14 shows the experimental probability density functions of $\tau_{\rm ch}$ for two example channels 186.65 THz ($\circ$) and 188.15 THz ($\blacktriangledown$). The data shown were collected in over 60 h of measurements, 10 h of which is shown on Fig. 11. The fiber passed through two huts (twice through one of them) experiencing strong temperature oscillations, so we surmise that during these measurements, we had a system with effectively only five active hinges [48]. Rapid reorientation of the hinges insured that we assembled a few hundred statistically independent samples during the measurement interval. The plot clearly demonstrates that the DGD at each frequency exhibits a distinct statistical distribution. The time-averaged DGD of these two channels is $\langle\tau_{\rm ch}\rangle_{\rm time} = 1.8$ and 1.0 ps for 186.65 and 188.15 THz, respectively. Other channels (our experimental frequency range was 186.5–188.5 THz) had mean values between these two cases. The measured DGD spectra can be divided into several correlated spectral bands of $\approx$0.3 THz width. DGD values taken at frequencies further apart than this display distributions that may have noticeably different mean values $\langle\tau_{\rm ch}\rangle_{\rm time}$. A similar behavior was observed on all data sets taken on different system configurations and different fiber strands as long as there were temperature variations driving the hinges [49], [50]. In addition, other field and numerical experiments [43], [44], [54] demonstrated related trends, as shown, for example, in Figs. 7 and 8.

Experimental determination of the exact shape of each channel's DGD time distributions is a nearly insurmountable task due to the limited number of DGD samples. However, each of such distributions could be approximated by a known distribution of a PMD emulator with sections of fixed magnitude. This approximation is valid under the following two conditions, namely 1) the buried fiber sections are assumed to remain fixed, and 2) the hinges are assumed to sample all of their accessible states. Fig. 15 plots these probability distribution functions for several emulators. Here, six numbers representing six fixed-section lengths were randomly drawn from a Maxwellian distribution with rms value $\tau_{\rm rms} = 1/\sqrt{6}$. Then, an analytical expression derived by Antonelli and Mecozzi [56] was used to compute the distributions. Different colors correspond to different section sets, each containing six randomly drawn numbers. Note the two important features, namely 1) the variations between different distributions and 2) the truncation of pdf at a finite τ.

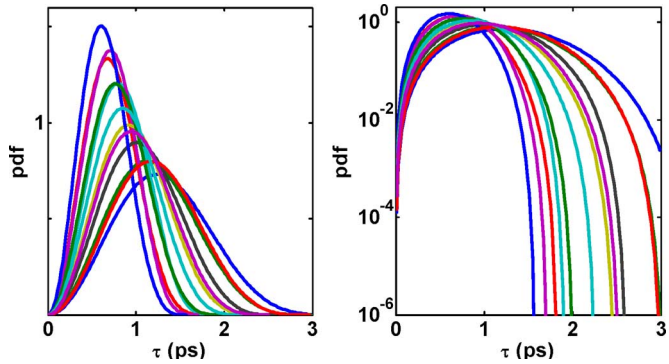

Fig. 15. Analytical probability distribution functions for a fixed-length-section emulator [56]. Different colors represent different choice of the fixed-length sections (see text). Note the variations between different distributions and the truncation of pdf at a finite τ: Only one distribution extends beyond 3 ps.

VII. PMD Outages Revisited

The existence of the channel-specific temporal DGD distribution has significant implications for the statistics of system outages. Recently, Boroditsky *et al.* showed via simulations that the outage statistics of a system with a finite fixed number of polarization rotation points (i.e., hinges) differs from what one would expect from a truly Maxwellian system, namely every channel has its own outage probability [57]. In a system with hinges, some channels will have an outage probability lower than the one expected from a Maxwellian distribution and will be more reliable, while other channels will have higher outage probabilities and will be prone to frequent outages. Furthermore, it turns out that a significant fraction of channels are *guaranteed* to be outage free for long periods of time, as long as the sections of the route between hinges do not change. This last property follows directly from the pdf's truncation at a finite τ: The PMD vector cannot be longer than the sum of the (relatively fixed) buried section PMDs.

In addition to DGD, a more realistic outage calculation should, of course, encompass variable launch conditions, receiver properties [58], [59] and, possibly, the effects of higher-order PMD [60]. The preliminary outage calculation for the hinge model [49], [57], [61], for simplicity, defined the outage probability of a given channel as the probability for its instantaneous DGD to exceed a certain maximum value. Consequently, the outage probability is reduced to the area under the tail of the DGD's pdf. Interestingly, a more rigorous analysis proposed by Kogelnik *et al.* (to be discussed below) exhibits similar qualitative behavior [62]. Both calculations were greatly simplified due to the prior derivation of an analytical expression for the probability distributions functions of an arbitrary multisection PMD emulator [56]. Indeed, in the framework of the hinge model with buried sections fixed in time, the time-domain DGD distribution for every channel is given by the pdf of a corresponding channel-specific emulator. To quantify the analysis here, we will refer to two complementary measures, namely 1) the compliant capacity fraction (CCF) and 2) the

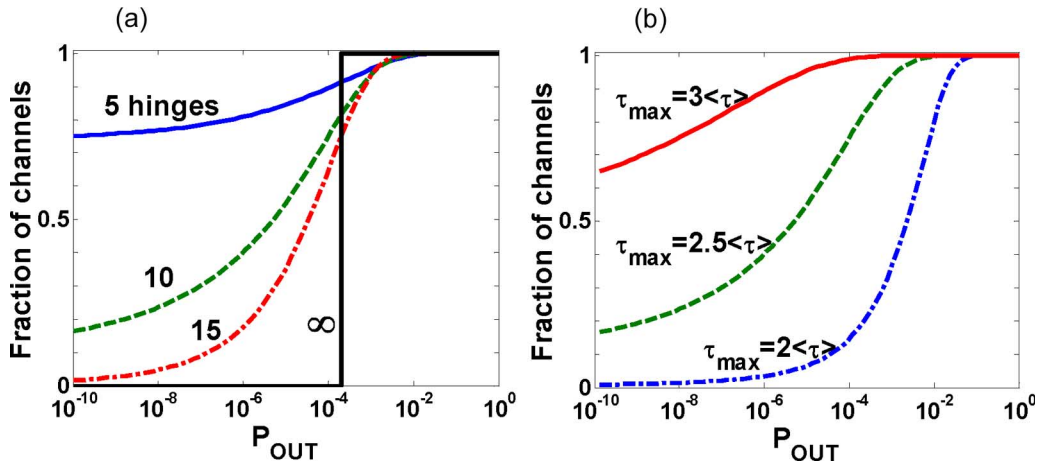

Fig. 16. (a) Distribution of the outage probability among channels in a system with the same values of the maximum DGD but different number of hinges. (b) Fraction of channels with outage probability less than abscissa in a system with $N = 10$ hinges for various values $\tau_{\max}$ of the maximum DGD tolerated by a receiver. From [57].

noncompliant capacity ratio (NCR) [62], to describe a fraction of channels with outage probability smaller or larger, respectively, than the outage specification.

A. Compliant Capacity Fraction

The cumulative probability for outages P_{out} of a system with maximum tolerable DGD $\tau_{\max} = 2.5\tau_{\text{rms}}$ for differing numbers of hinges in a system $(N = 5, 10, 15)$ [57] is plotted in Fig. 16(a). In other words, it shows the fraction of channels whose outage probabilities are smaller than the value of the desired outage probability on the horizontal axis P_{out}. This plotted quantity is the CCF. As before, an outage probability, P_{out}, is the probability for the instantaneous DGD value τ to exceed a certain threshold $\tau_{\max}$. For example, if a system has ten hinges, and the desired outage probability is 10^{-6}, according to the hinge model, we expect that 40% of the channels will have an outage probability better than 10^{-6}, while the remaining 60% will not satisfy the outage specification. Given that the range of outage probabilities of interest covers several orders of magnitude, P_{out} is plotted on a logarithmic scale. Clearly, as the number of degrees of freedom increases, the system starts to behave more like a Maxwellian system, and plots in Fig. 16(a) tend toward the step-like shape corresponding to the situation when all channels have identical Maxwellian statistics in time and the same outage probability: $2 \cdot 10^{-4}$ in this case. Approaching it from another direction, we can think of the reduction of degrees of freedom in a system as "washing out" the step-function describing the outage probability. As a result, some channels have an outage probability smaller than, but some channels have an outage probability larger than, that expected from a Maxwellian distribution.

The concept of CCF is further illustrated in Fig. 16(b), which plots CCF again as a function of specified outage probability P_{out} but now for a system with ten hinges for three different PMD tolerance levels $\tau_{\max}$. For a finite number of hinges, a significant number of channels have a very small outage probability due to the truncation effect from the finite number of sections. However, there is a small fraction of channels (with relatively large individual sections) that exceeds the conventional threshold of $\tau_{\max} = 3\tau_{\text{rms}}$ frequently and, thus, has an outage probability significantly larger than 4.2×10^{-5}. In fact, 90% of the channels will have an outage probability less than 4.2×10^{-5} for a realistic case of 15 or fewer hinges and $\tau_{\max} = 3\tau_{\text{rms}}$. Interestingly, at the limit of $P_{\text{out}} = 0$, the curves tend to a constant nonzero value, corresponding to the fraction of completely outage-free channels. For these channels, the arithmetical sum of "frozen" PMD vectors does not exceed the threshold value $\tau_{\max}$.

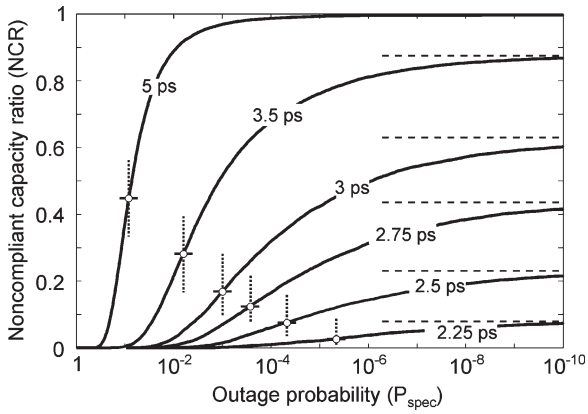

Fig. 17. NCR as a function of P_{spec} for links with five hinges, 1-dB margin, and 40-Gb/s NRZ modulation. The link's mean DGD is indicated on each curve. The dotted lines indicate the traditional outage probabilities obtained from Maxwellian distribution. The dashed horizontal lines are the asymptotes of zero outage probability for each mean DGD. From [62].

B. Noncompliant Capacity Ratio

The outage probabilities for the hinge model were analyzed more rigorously in [62] using the outage map approach and thus taking the receiver design into account. Another metric called NCR was introduced in [62]. For historical reasons, the outage scale is chosen in the direction opposite to that in Figs. 16 and 17. Furthermore, since the NCR is complementary to the CCF, plots in Figs. 16 and 17 can be most easily compared by rotating either one by 180°.

The simulation results for the NRZ modulation format and a selected number of mean DGDs are shown in Fig. 17 as a

function of the specified outage for a typical 40 Gb/s system with five hinges and receiver maximum PMD tolerance of $\tau_{\max} \sim 6.9$ ps. Plots for the RZ format look similar except that the corresponding mean DGDs are about twice as large. Compare the results shown in Fig. 17 for the hinge model with the traditional results corresponding to an infinite number of hinges. For the latter, there is a distinct outage probability, marked by a vertical dotted line, for each specified mean DGD, marked by an open circle. In the traditional case, all spectral bands have the same outage characteristics. Therefore, as discussed above, for a given mean DGD, e.g., 2.5 ps, all bands will either satisfy a specified outage or violate it. There will be an abrupt transition from NCR $= 0$ to NCR $= 1$. This transition occurs at the outage value marked by the dotted line, i.e., all bands are guaranteed an outage probability of less than about 5×10^{-5} as long as $\Delta\overline{\tau} = 2.5$ ps or less. As the number of hinges increases from the five-hinge case discussed below, the NCR curves get steeper and approach the vertical dotted lines.

C. New Possibilities to Cope With PMD Outages

This new way of looking at outages highlights the utmost importance of in-service PMD monitoring techniques [63]–[65] and possibly opens a new paradigm in addressing the PMD impairment altogether. Indeed, if it was possible to know which channels are outage free, these channels could be used for high-availability services. Alternatively, increasing the tolerance toward PMD either by improving the system or by choosing a slightly better fiber should increase the fraction of outage-free channels. For example, as follows from Fig. 16, this fraction can be tuned from 75% to 96% by changing the tolerance from $\tau_{\max} = 2.5\tau_{\rm rms}$ to $\tau_{\max} = 3\tau_{\rm rms}$ for a system with ten hinges. On the other hand, the fiber constraints could be relaxed. If a route has 15 or fewer hinges, then by using tunable transponders (currently an emerging technology), the PMD outage problem could be solved by simply underutilizing the overall capacity by as little as 10% and using the 90% of "good" channels in the system. Finally, since service level agreements are typically written in terms of the outage per month or per year, it might make sense to artificially add extra degrees of freedom (say, several slow polarization scramblers mid-span) to force more predictable PMD dynamics closer to those described by a Maxwellian distribution over a desired timescale.

VIII. Conclusion and Goals for Future Study

In this paper, we reviewed a wealth of experimental data that point to the long-term stability of DGD in buried fiber-optic cables and that identify localized sections of the links, either exposed sections of fibers or in-line components, as the source of the most DGD important time dynamics up to month-long time scales. Important features as well as the most significant implication of the results of reviewed experiments were summarized in a simple empirical hinge model. This model serves as a physical description and a calculational basis for new analyses of outage probabilities. The experimental evidence and analytic results have changed the fundamental view of system vulnerability to PMD: Instead of all channels being equally vulnerable at all times to PMD-induced outages, systems with hinges are expected to possess a significant number of channels that would be outage free for long time periods, and a smaller number of channels that should experience frequent outages. Further studies of the dynamics of completely buried sections and hinges, with the aim of more accurately determining the characteristic timescales, are needed to assess the limitations of the early models. Such studies, augmented with more sophisticated outage models and strategies to use them, should be an important part of our efforts to remove PMD as an impediment to the ever-increasing transmission throughputs.

Appendix
Uncertainty of Calculated RMS DGD of a Multispan Route

Since the rms DGD value $\tau_{\rm rms}$ serves as the principal metric describing a fiber system's PMD properties, telecom carriers routinely characterize their installed fiber plants by measuring the rms DGD value of each individual fiber span (span length is about 80 km) in a system, that is, $\tau_i^{\rm rms}$ for the ith span in the overall link. As discussed in Section III, what is experimentally attainable is not the *true* rms DGD value of an installed low-PMD fiber span $\tau_i^{\rm rms}$ but rather its statistically uncertain estimate τ_i [31], [32]. Interestingly, if spectrally resolved measurements are used for rms DGD estimation, the estimate's variance can be reduced by 50% using statistical properties of the second-order PMD [66]. Normally, when many spans are concatenated to form a long route, the multispan DGD value τ_Σ is *calculated* based on experimentally *measured* individual span values τ_i according to the formula $\tau_\Sigma^2 = \Sigma\tau_i^2$. Unavoidable measurement ambiguity in each τ_i causes, in turn, the uncertainty in τ_Σ. A question vital to any carrier is by how much the computed value τ_Σ is likely to differ from the true rms value $\tau_\Sigma^{\rm rms}$. Below, we present simple arguments allowing us to estimate this uncertainty.

Mathematically, this problem can be reformulated as finding a standard deviation σ_Σ of an algebraic function $\tau_\Sigma = \tau_\Sigma(\tau_1, \tau_2, \ldots, \tau_N)$ of N random variables τ_i, each of which has a *known* standard deviation σ_i (recall that for the fixed measurement bandwidth $\sigma_i \approx \tau_i^{1/2}$ [32]). The variables τ_i are statistically independent as they represent different fibers. Thus, the following formula can be applied [67]:

$$\sigma_\Sigma^2 = \sum \left(\frac{\partial\tau_\Sigma}{\partial\tau_i}\right)^2 \sigma_i^2 = \frac{\sum \tau_i^2\sigma_i^2}{\sum \tau_i^2}. \tag{7}$$

It is illustrative to examine two important asymptotic cases. First, let us consider identical spans. In other words, the mean values and standard deviations of measured variables τ_i are identical among spans, i.e., for every i, $\langle\tau_i\rangle = \tau_0$ and $\sigma_i = \sigma_0$. In this case, the expression in (7) simplifies to

$$\sigma_\Sigma^2 = \frac{\sum \tau_0^2\sigma_0^2}{\sum \tau_0^2} = \sigma_0^2. \tag{8}$$

Therefore, $\sigma_\Sigma = \sigma_0$, i.e., the *absolute* error with which the calculated τ_Σ approximates the true value τ_Σ does not accumulate with the number of spans N. But since the value $\tau_\Sigma^{\rm rms}$ itself

grows as $\sqrt{N}(\tau_\Sigma = \sqrt{N\tau_0})$, the *relative* error becomes smaller for larger N.

Another important situation is when one span's DGD dominates the rest; therefore, for every $i \neq k$ $\langle\tau_i\rangle \ll \langle\tau_k\rangle$, and, correspondingly, $\langle\sigma_i\rangle \ll \langle\sigma_k\rangle$. It follows from (7) that $\sigma_\Sigma = \sigma_k$. Indeed

$$\sigma_\Sigma^2 = \frac{\sum \tau_i^2\sigma_i^2}{\sum \tau_i^2} \approx \frac{\tau_k^2\sigma_k^2}{\tau_k^2} = \sigma_k^2. \tag{9}$$

The resulting absolute aggregate error σ_Σ is equal to that of the worst span σ_k and, once again, is independent of the number of spans N.

In the two cases presented above, we illustrated that the *absolute* uncertainty of the computed value τ_Σ is either approximately equal to each span's uncertainty or to that of the principal contributor of the DGD. More realistic situations are in between the two cases. Generalizing, we conclude that despite huge relative errors inherent to each τ_i, the relative error for τ_Σ decreases roughly as $\sqrt{N}$ with the number of spans N. The conclusion is somewhat counterintuitive: to obtain a multispan rms DGD value $\tau_\Sigma^{\rm rms}$ with better precision, a route should be divided into a larger number of shorter spans, and each of them measured individually. Although each span's measurements will be less precise this way, the final result for $\tau_\Sigma^2 = \Sigma\tau_i^2$ improves due to the larger number of measurements.

ACKNOWLEDGMENT

The authors would like to thank P. Magill, who was a collaborator on many experiments described in this paper, and several groups that shared their data with us, particularly C. Allen, R. Leppla, and D. Petersson. Over the last several years, the authors enjoyed invaluable discussions with many friends and colleagues. The authors would also like to thank C. Antonelli, G. Carter, K. Cornick, A. Eyal, A. Galtarossa, R. Jopson, M. Karlsson, H. Kogelnik, A. Mecozzi, C. Menyuk, L. Nelson, L. Palmieri, M. Santagiustina, M. Schiano, M. Shtaif, A. Willner, and P. Winzer.

REFERENCES

[1] C. D. Poole and J. A. Nagel, "Polarization effects in lightwave systems," in *Optical Fiber Telecommunications IIIA*, I. P. Kaminow and T. L. Koch, Eds. San Diego, CA: Academic, 1997, pp. 114–161.

[2] J. P. Gordon and H. Kogelnik, "PMD fundamentals: Polarization mode dispersion in optical fibers," *Proc. Nat. Acad. Sci. USA*, vol. 97, no. 9, pp. 4541–4550, Apr. 2000.

[3] H. Kogelnik, R. M. Jopson, and L. E. Nelson, "Polarization mode dispersion," in *Optical Fiber Telecommunications IVB*, I. P. Kaminow and T. Li, Eds. San Diego, CA: Academic, 2002, pp. 725–861.

[4] C. D. Poole and R. E. Wagner, "Phenomenological approach to polarization dispersion in long single-mode fibers," *Electron. Lett.*, vol. 22, no. 19, pp. 1029–1030, Sep. 1986.

[5] J. N Damask, *Polarization Optics in Telecommunications*. New York: Springer, 2004.

[6] A. Galtarossa and C. R. Menyuk, Eds., *Polarization Mode Dispersion*. New York: Springer, 2005.

[7] R. M. Jopson, L. E. Nelson, and H. Kogelnik, "Measurement of second-order polarization-mode dispersion vectors in optical fibers," *IEEE Photon. Technol. Lett.*, vol. 11, no. 9, pp. 1153–1155, Sep. 1999.

[8] R. Ulrich, "Representation of codirectional coupled waves," *Opt. Lett.*, vol. 5, pp. 109–111, 1977.

[9] N. J. Frigo, "A generalized geometrical representation of coupled mode theory," *IEEE J. Quantum Electron.*, vol. QE-22, no. 11, pp. 2121–2140, Nov. 1986.

[10] C. D. Poole, J. H. Winters, and J. A. Nagel, "Dynamical equation for polarization dispersion," *Opt. Lett.*, vol. 16, no. 6, pp. 372–374, Mar. 1991.

[11] F. Curti, B. Daino, G. DeMarchis, and F. Matera, "Statistical treatment of the evolution of the principal states of polarization in single-mode fibers," *J. Lightw. Technol.*, vol. 8, no. 8, pp. 1162–1166, Aug. 1990.

[12] G. J. Foschini and C. D. Poole, "Statistical theory of polarization dispersion in single mode fibers," *J. Lightw. Technol.*, vol. 9, no. 11, pp. 1439–1456, Nov. 1991.

[13] C. D. Poole and C. R. Giles, "Polarization-dependent pulse compression and broadening due to polarization dispersion in dispersion-shifted fiber," *Opt. Lett.*, vol. 13, no. 2, pp. 155–157, Feb. 1988.

[14] C. D. Poole, R. W. Tkach, A. R. Chraplyvy, and D. A. Fishman, "Fading in lightwave systems due to polarization-mode dispersion," *IEEE Photon. Technol. Lett.*, vol. 3, no. 1, pp. 68–70, Jan. 1991.

[15] C. De Angelis, A. Galtarossa, G. Gianello, F. Matera, and M. Schiano, "Time evolution of polarization mode dispersion in long terrestrial links," *J. Lightw. Technol.*, vol. 10, no. 5, pp. 552–555, May 1992.

[16] L. M. Gleeson, E. S. R. Sikora, and M. J. O'Mahoney, "Experimental and numerical investigation into the penalties induced by second order polarization mode dispersion at 10 Gb/s," in *Proc. ECOC*, 1997, vol. 1, pp. 15–18.

[17] H. Bülow and G. Veith, "Temporal dynamics of error-rate degradation induced by polarization mode dispersion fluctuation of a field fiber link," in *Proc. ECOC*, 1997, vol. 1, pp. 115–118.

[18] J. Cameron, X. Bao, and J. Stears, "Time evolution of polarization mode dispersion for aerial and buried cables," in *Proc. OFC*, 1998, pp. 240–241, Paper WM51.

[19] J. Cameron, L. Chen, X. Bao, and J. Stears, "Time evolution of polarization mode dispersion in optical fibers," *IEEE Photon. Technol. Lett.*, vol. 10, no. 9, pp. 1265–1267, Sep. 1998.

[20] W. Weiershausen, H. Schöll, F. Küppers, R. Leppla, B. Hein, H. Burkhard, E. Lach, and G. Veith, "40 Gb/s field test on an installed fiber link with high PMD and investigation of differential group delay impact on transmission performance," in *Proc. OFC*, 1999, vol. 3, pp. 125–127, Paper ThI5.

[21] M. Karlsson, M. J. Brentel, and P. Andrekson, "Long-term measurement of PMD and polarization drift in installed fibers," *J. Lightw. Technol.*, vol. 18, no. 7, pp. 941–951, Jul. 2000.

[22] J. A. Nagel, M. W. Chbat, L. D. Garrett, J. P. Soigé, N. A. Weaver, B. M. Desthieux, H. Bülow, A. R. McCormick, and R. M. Derosier, "Long-term PMD mitigation at 10 Gb/s and time dynamics over high-PMD installed fiber," in *Proc. ECOC*, 2000, vol. 2, pp. 31–32.

[23] C. T. Allen, P. K. Kondamuri, D. L. Richards, and D. C. Hague, "Measured temporal and spectral PMD characteristics and their implications for network-level mitigation approaches," *J. Lightw. Technol.*, vol. 21, no. 1, pp. 79–86, Jan. 2003.

[24] D. L. Peterson, B. C. Ward, K. B. Rochford, P. J. Leo, and G. Simer, "Polarization mode dispersion compensator field trial and fiber field characterization," *Opt. Express*, vol. 10, no. 14, pp. 614–621, Jul. 2002.

[25] H. Bülow, W. Baumert, H. Schmuck, F. Mohr, T. Schulz, F. Küppers, and W. Weinershausen, "Measurement of the maximum speed of PMD fluctuation in installed field fiber," in *Proc. OFC*, 1999, pp. 83–85, Paper WE4.

[26] P. M. Krummrich and K. Kotten, "Extremely fast (microsecond scale) polarization changes in high speed long haul WDM transmission systems," in *Proc. OFC*, 2004, Paper FI3.

[27] P. M. Krummrich, E.-D. Schmidt, W. Weinershausen, and A. Mattheus, "Field trial results on statistics of fast polarization changes in long haul WDM transmission systems," in *Proc. OFC*, 2005, Paper OThT6.

[28] M. Boroditsky, M. Brodsky, P. D. Magill, and H. Rosenfeldt, "Polarization dynamics in installed fiberoptic systems," in *Proc. LEOS Annu. Meeting*, 2005, pp. 414–415, Paper TuCC1.

[29] M. Brodsky, M. Boroditsky, P. D. Magill, N. J. Frigo, and M. Tur, "A 'Hinge' model for the temporal dynamics of polarization mode dispersion," in *Proc. LEOS Annu. Meeting*, 2004, pp. 90–91, Paper MJ5.

[30] N. Gisin, J. P. Von der Weid, and J. P. Pellaux, "Polarization mode dispersion of short and long single-mode fibers," *J. Lightw. Technol.*, vol. 9, no. 7, pp. 821–827, Jul. 1991.

[31] N. Gisin, B. Gisin, J. P. Von der Weid, and R. Passy, "How accurately can one measure a statistical quantity like polarization-mode dispersion?" *IEEE Photon. Technol. Lett.,* vol. 8, no. 12, pp. 1671–1673, Dec. 1996.

[32] M. Shtaif and A. Mecozzi, "Study of the frequency autocorrelation of the differential group delay in fibers with polarization mode dispersion," *Opt. Lett.*, vol. 25, no. 10, pp. 707–709, May 2000.

[33] M. Karlsson and J. Brentel, "Autocorrelation function of the polarization mode dispersion vector," *Opt. Lett.*, vol. 24, no. 14, pp. 939–941, Jul. 1999.

[34] P. D. Magill and M. Brodsky, "PMD of installed fiber—An overview," in *Proc. LEOS PMD Summer Top. Meeting*, 2003, pp. 7–8. Paper MB2.2.
[35] M. Brodsky, P. D. Magill, and N. J. Frigo, "'Long-term' PMD characterization of installed fibers—How much time is adequate?" in *Proc. OFC*, 2004, Paper FI5
[36] D. L. Harris, P. K. Kondamuri, J. Pan, and C. Allen, "Temperature dependence of wavelength-averaged DGD on different buried fibers," in *Proc. LEOS Annu. Meeting*, 2004, pp. 84–85, Paper MJ2.
[37] R. Caponi, B. Riposati, A. Rossaro, and M. Schiano, "WDM design issues with highly correlated PMD spectra of buried optical cables," in *Proc. OFC*, 2002, pp. 453–455, Paper ThI5.
[38] J. Rasmussen, "Automatic PMD and chromatic dispersion compensation in high capacity transmission," in *Proc. LEOS PMD Summer Top. Meeting*, 2003, pp. 47–48, Paper TuB3.4.
[39] A. Nespola, S. Abrate, P. Poggiolini, and M. Magri, "Long term PMD compensation of installed G.652 fibers in a metropolitan network," in *Proc. OFC*, 2005, Paper JWA1.
[40] M. Brodsky, P. D. Magill, and N. J. Frigo, "Evidence for parametric dependence of PMD on temperature in installed 0.05 ps/km1/2 fiber," in *Proc. ECOC*, 2002, vol. 4, Paper 9.3.2.
[41] ——, "Polarization-mode dispersion of installed recent vintage fiber as a parametric function of temperature," *IEEE Photon. Technol. Lett.*, vol. 16, no. 1, pp. 209–211, Jan. 2004.
[42] N. J. Frigo and J. A. Nagel, unpublished.
[43] M. Brodsky and M. Tur, unpublished.
[44] P. K. Kondamuri, C. Allen, and D. L. Richards, "Study of variation of the Laplacian parameter of DGD time derivative with fiber length using measured DGD data," in *Proc. Symp. Opt. Fiber Meas.*, 2004, pp. 91–94.
[45] C. Allen, P. K. Kondamuri, D. L. Richards, and D. C. Hague, "Analysis and comparison of measured DGD data on buried single-mode fibers," in *Proc. Symp. Opt. Fiber Meas.*, 2002, pp. 195–198.
[46] M. Birk, L. Raddatz, D. Fishman, S. Woodward, and P. D. Magill, "Field trial of end-to-end OC-768 transmission using 9 WDM channels over 1000 km of installed fiber," in *Proc. OFC*, 2003, vol. 1, pp. 290–291.
[47] M. Brodsky, M. Boroditsky, P. D. Magill, N. J. Frigo, and M. Tur, "Field PMD measurements through a commercial, Raman-amplified ULH transmission system," in *Proc. LEOS PMD Summer Top. Meeting*, 2003, pp. 15–16, Paper MB3.3.
[48] ——. (2004, Jun.). "Physical mechanism for polarization mode dispersion temporal dynamics," *IEEE LEOS Newslett.*, pp. 4–6, vol. 18, no. 3. [Online]. Available: http://www.ieee.org/organizations/pubs/newsletters/leos/jun04/polarization.html
[49] ——, "Channel-to-channel variation of non-Maxwellian statistics of DGD in a field installed system," in *Proc. ECOC*, 2004, vol. 3, pp. 306–309, Paper We1.4.1.
[50] ——. (2005, May). "Persistence of spectral variations in DGD statistics," *Opt. Express*, pp. 4090–4095, vol. 13, no. 11. [Online]. Available: http://www.opticsexpress.org/abstract.ft3/min?URI=OPEX-13-11-4090
[51] M. Boroditsky, M. Brodsky, N. J. Frigo, P. D. Magill, and L. Raddatz, "Technique for *in situ* measurements of polarization mode dispersion," in *Proc. OFC*, 2003, vol. 1, pp. 224–225, Paper TuK1.
[52] ——, "In-service measurements of polarization mode dispersion and correlation to bit-error rate," *IEEE Photon. Technol. Lett.*, vol. 15, no. 4, pp. 572–574, Apr. 2003.
[53] W. Weiershausen, R. Leppla, F. Rumpf, R. Herber, A. Mattheus, A. Gladisch, A. Hirano, Y. Kisaka, Y. Miyamoto, S. Kuwahara, M. Yoneyama, and M. Tomizawa, "PMD outage measurements in a joint field trial of a 43-Gb/s NTT WDM transmission system within DT's installed fiber environment," in *Proc. OFC*, 2004, Paper WP3.
[54] R. Leppla, S. Vorbeck, D. Goelz, S. Salaun, M. Joindot, and R. Glatty, "Optical channel model for system outage probability analysis based on PMD measurements of installed WDM links and its components," in *Proc. SPIE*, 2005, vol. 6012, pp. 167–182.
[55] M. Brodsky, J. Martinez, N. J. Frigo, and A. Sirenko, "Dispersion compensation module as a polarization hinge," in *Proc. ECOC*, 2005, pp. 335–336, Paper We 1.3.2 .
[56] C. Antonelli and A. Mecozzi, "Statistics of the DGD in PMD emulators," *IEEE Photon. Technol. Lett.*, vol. 16, no. 8, pp. 1840–1842, Aug. 2004.
[57] M. Boroditsky, M. Brodsky, N. J. Frigo, P. D. Magill, C. Antonelli, and A. Mecozzi, "Outage probability for fiber routes with finite number of degrees of freedom," *IEEE Photon. Technol. Lett.*, vol. 17, no. 2, pp. 345–347, Feb. 2005.
[58] P. J. Winzer, H. Kogelnik, C. H. Kim, H. Kim, R. M. Jopson, L. E. Nelson, and K. Ramanan, "Receiver impact on first-order PMD outage," *IEEE Photon. Technol. Lett.*, vol. 15, no. 10, pp. 1482–1484, Oct. 2003.
[59] P. J. Winzer, H. Kogelnik, and K. Ramanan, "Precise outage specifications for first-order PMD," *IEEE Photon. Technol. Lett.*, vol. 16, no. 2, pp. 449–451, Feb. 2004.
[60] M. Shtaif and M. Boroditsky, "The effect of the frequency dependence of PMD on the performance of optical communications systems," *IEEE Photon. Technol. Lett.*, vol. 15, no. 10, pp. 1369–1371, Oct. 2003.
[61] A. Mecozzi, C. Antonelli, M. Boroditsky, and M. Brodsky, "Characterization of the time dependence of polarization mode dispersion," *Opt. Lett.*, vol. 29, no. 22, pp. 2599–2601, Nov. 2004.
[62] H. Kogelnik, P. J. Winzer, L. E. Nelson, R. M. Jopson, M. Boroditsky, and M. Brodsky, "First-order PMD outage for the hinge model," *IEEE Photon. Technol. Lett.*, vol. 17, no. 6, pp. 1208–1210, Jun. 2005.
[63] M. Boroditsky, K. Cornick, C. Antonelli, M. Brodsky, S. Dods, N. J. Frigo, and P. D. Magill, "Comparison of system penalties from first- and multiorder polarization-mode dispersion," *IEEE Photon. Technol. Lett.*, vol. 17, no. 8, pp. 1650–1652, Aug. 2005.
[64] S. X. Wang, A. M. Weiner, M. Boroditsky, and M. Brodsky, "Monitoring PMD-induced penalty and other system performance metrics via a high-speed spectral polarimeter," *IEEE Photon. Technol. Lett.*, vol. 18, no. 16, pp. 1753–1755, Aug. 2006.
[65] K. E. Cornick, M. Boroditsky, S. Finch, S. D. Dods, and P. M. Farrell, "Experimental comparison of PMD-induced system penalty models," *IEEE Photon. Technol. Lett.*, vol. 18, no. 10, pp. 1149–1151, May 2006.
[66] M. Boroditsky, M. Brodsky, P. Magill, N. J. Frigo, and M. Shtaif, "Improving the accuracy of mean DGD estimates by analysis of second-order PMD statistics," *IEEE Photon. Technol. Lett.*, vol. 16, no. 3, pp. 792–794, 2004.
[67] D. C. Baird, *Experimentation: An Introduction to Measurement Theory and Experiment Design*. Englewood Cliffs, NJ: Prentice-Hall, 1962.

Misha Brodsky (M'05) received the Diploma (M.Sc.) degree from St. Petersburg Technical University, St. Petersburg, Russia, in 1992 and the Ph.D. degree in physics from Massachusetts Institute of Technology, Cambridge, in 2000.

For a year, he was a Research Associate with Ioffe Institute, where he studied properties of multiple-quantum-well structures. His graduate school research was focused on the behavior of strongly correlated electrons in low-dimensional systems in the quantum Hall regime. During graduate school, he spent the summer of 1997 with Bell Laboratories, Murray Hill, NJ, where he worked on novel photodectors. In 2000, he joined the Optical System Research Division, AT&T Laboratories, Middletown, NJ, as a Senior Member of Technical Staff. He has worked in various physical-layer telecom research areas including WDM metro architectures, polarization-mode dispersion, and, more recently, quantum key distribution.

Dr. Brodsky is a member of the American Physical Society and the Optical Society of America.

Nicholas J. Frigo (M'82–S'82–SM'04–F'06) received the B.A. degree in physics from Claremont-McKenna College, Claremont, CA, and the M.S. and Ph.D. degrees in physics from Cornell University, Ithaca, NY.

In 1982, he was a Research Physicist with the Optical Sciences Division, U.S. Naval Research Laboratory, Washington, DC, and worked on fiber-optic sensors for six years. After two years as a Research Department Head with Litton Industries, he joined AT&T Bell Labs in 1990, where he initially worked on fundamental impairments for fiber-optic TV transmission and on long-reach undersea fiber-optic systems. While at Bell Labs, he began investigating passive optical network architectures for fiber-to-the-home architectures and was promoted to Distinguished Member of Technical Staff. After the AT&T trivestiture, he was with AT&T Labs-Research, where he worked on optical access architectures for business customers, polarization mode dispersion, network diagnostic techniques, and various strategic issues. At AT&T, he held positions as Technology Leader and as Division Manager of the Optical Systems Department. Since August 2005, he has been with the Physics Department, United States Naval Academy, Annapolis, MD, and is the first Michelson Professor of physics. He has authored or coauthored over 90 conference presentations, including 25 invited talks, over 60 publications, and is the inventor or coinventor on over 40 U.S. patents.

Prof. Frigo has served on various Technical Program Committees and has been an Associate Editor of *Photonics Technology Letters*.

Misha Boroditsky (SM'06) received the M.S. degree in applied physics from St. Petersburg Polytechnic Institute, St. Petersburg, Russia, in 1993 and the Ph.D. degree in physics from the University of California, Los Angeles, in 1999. His Ph.D. dissertation was on the modification of spontaneous emissions in photonic crystals.

After graduation, he worked for more than six years with the Optical Systems Research Department, AT&T Laboratories, on various aspects of access architectures, ultrafast optical packet switching, and polarization-mode dispersion. Since May 2006, he has been working in the field of quantitative finance with the Statistical Arbitrage Group, Knight Equity Markets, Jersey City, NJ. He has authored or coauthored more than 50 publications. He is the holder of six patents.

Dr. Boroditsky served on the Optical Fiber Communications Technical Committee from 2004 to 2006 and was the Lasers and Electro-Optics Society Meeting Committee Chair for 2005–2006.

Moshe Tur (M'87–SM'94–F'98) received the B.Sc. degree in mathematics and physics from the Hebrew University, Jerusalem, Israel, the M.Sc. degree in applied physics from the Weizmann Institute of Science, Rehovot, Israel, and the Ph.D. degree from Tel Aviv University, Tel Aviv, Israel, in 1981.

From 1981 to 1983, he was a Post-Doctoral Fellow and then a Research Associate with the Information System Laboratory and the Edward L. Ginzton Laboratory, Stanford University, Stanford, CA, where he participated in the development of new architectures for single-mode fiber-optic signal processing and investigated the effect of laser phase noise on such processors. He is currently a Gordon Professor of electrical engineering with the School of Electrical Engineering, Department of Indisciplinary Studies, Faculty of Engineering, Tel Aviv University, where he has established a fiber-optic sensing and communication laboratory. He authored or coauthored more than 250 journal and conference technical papers with emphasis on fiber-optic bit-rate limiters, fiber lasers, fiber-optic sensor arrays, the statistics of phase-induced intensity noise in fiber-optic systems, fiber sensing in smart structures, fiber Bragg gratings, polarization mode dispersion, microwave photonics, and advanced fiber-optic communication systems.

Dr. Tur is a Fellow of the Optical Society of America.